Ultraprecision imaging and manipulation of plasmonic nanostructures by integrated nanoscopic correction (iNC)

*Yunbo Liu, Zhijia Zhang, Younggeun Park, Somin Eunice Lee**

Y. Liu, Z. Zhang

Department of Electrical & Computer Engineering

University of Michigan, Ann Arbor, MI 48109 USA

Dr. Y. Park

Department of Mechanical Engineering, Center for Integrative Research in Critical Care, University of Michigan, Ann Arbor, MI 48109 USA

Prof. S.E.Lee

Department of Electrical & Computer Engineering, Department of Biomedical Engineering, Biointerfaces Institute, Applied Physics, Macromolecular Science and Engineering

University of Michigan, Ann Arbor, MI 48109 USA

Keywords: plasmonics, multimodal super-resolution imaging, multimodal optical trapping

Abstract

Optical manipulation and imaging of nano-objects with nanometer precision is highly desirable for nanomaterial and biological studies due to inherent noninvasiveness. However, time constraints and current segregated experimental systems for nanoimaging and nanomanipulation

limits real-time super-resolution imaging with spatially enhanced manipulation. Here, we report an integrated nanoscopic correction (iNC) method to enable multimodal nanomanipulation-nanoimaging. The iNC consists of a multimodal voltage-tunable power modulator, polarization rotator, and polarizer. Using iNC, we demonstrate plasmonic nano-objects (gold nanorods) which are below diffraction limit can be distinguished by direct observation without post processing. Furthermore, we show such direct observations with enhanced nanometer spatial stability and millisecond high speed. We successfully demonstrate precise trapping and rapid rotation of gold nanorods with iNC. With non-invasive post-processing free nanoimaging and nanomanipulation, we anticipate iNC will make contributions in the nanomaterial and biological sciences requiring precision optics.

1. Introduction

Precise, direct delivery of editing components to a desired intracellular site (Figure 1) is considered to be essential for emerging precision medicine and gene editing, as editing activities must be spatially controlled to ensure efficacy[1]. Pioneering works in optical trapping have demonstrated controlled manipulation and assembly of objects[2]. Optical manipulation with imaging would be highly desirable for enabling precise, direct delivery of nano-objects carrying editing components. Recently, super-resolution optical imaging has allowed for bypassing the diffraction limit to observe spatial features of objects with exquisite detail. Super-resolution methods increase resolution by spectral separation of fluorophores, as employed in ground state depletion microscopy, stimulated emission depletion and reversible saturable optical fluorescence transitions[3–5]. Super-resolution methods also commonly increase resolution by temporal separation of fluorophores, as utilized in photoactivated localization microscopy, super-resolution optical fluctuation imaging, and stochastic optical reconstruction microscopy[6–8]. To achieve spectral and

temporal separation of fluorophores, super-resolution imaging can require as many as 10^5 images, taking as long as several hours to acquire a complete image stack[6]. Such time constraints, as well as segregated experimental systems, limit integration of real-time super-resolution imaging with spatially enhanced manipulation. Super-resolution imaging combined with manipulation of nano-objects are necessary to open new possibilities in nanomaterial and biological studies.

Alternatively, plasmonic nano-objects[9–23] undergo elastic scattering processes which are energy conserving and therefore hold great potential as probes with an unlimited photon budget for real-time super-resolution. Unlike conventional super-resolution approaches using spectral and temporal separation of fluorophores, the underlying principle here utilizes anisotropic plasmonic nano-objects which can be differentiated below the diffraction limit by polarization[24–30]. However, conventional implementations to rotate the polarization by mechanical means introduce beam deviations and subsequently result in spatial errors. When spatial errors reach the same size order as the objects-of-interest, positional information (nanometers) becomes obscured, limiting real-time super-resolution capabilities.

Here, we present an integrated nanoscopic correction (iNC) method to enable multimodal nanomanipulation-nanoimaging. The iNC consists of liquid crystal and fixed retarders to function as a multimodal voltage-tunable power modulator, polarization rotator, and polarizer. Systematic voltage control enables correction of beam deviations and dynamic modulation of the transmission polarization. The transmission polarization can be rapidly tuned for dynamic, highspeed nanoimaging and nanomanipulation. We show that the iNC can be switched between different modes (power modulator, polarization rotator, polarizer) with nanometer spatial precision. Using iNC, we demonstrate plasmonic nano-objects (gold nanorods) which are below diffraction limit can be distinguished by direct observation without post processing. Furthermore, we show such direct observations with nanometer spatial stability and millisecond high speed. To the best of our

knowledge, for the first time, the iNC directly visualize segregated nano-objects at the nanoscale without post-processing. We successfully demonstrate precise trapping and rapid rotation of gold nanorods with iNC.

2. Results & Discussion

2.1. Spatially enhanced nanoimaging by iNC

Integrated nanoscopic correction (iNC) is necessary to enable real-time super resolution imaging. For this purpose, we built a fully integrated active control system comprised of a series of liquid crystal (LC) and fixed retarders allowing for multimodal operations (Figure 2). As a first step, the iNC was operated in the polarizer mode to image plasmonic nano-objects. In this operation mode, the output Stokes parameters of the iNC can be theoretically calculated from the following Mueller matrix as

$$\begin{bmatrix} I \\ Q \\ U \\ V \end{bmatrix} = \frac{1}{2}\begin{bmatrix} 1 & -cos\delta_1 & -sin\delta_1 & 0 \\ -cos\delta_2 & cos\delta_1 cos\delta_2 & sin\delta_1 cos\delta_2 & 0 \\ -sin\delta_2 & cos\delta_1 sin\delta_2 & sin\delta_1 sin\delta_2 & 0 \\ 0 & 0 & 0 & 0 \end{bmatrix}\begin{bmatrix} I_s \\ Q_s \\ U_s \\ V_s \end{bmatrix} \quad (1)$$

$$= \frac{1}{2}\begin{bmatrix} 1 - cos\delta_1 \\ \cos\delta_2(cos\delta_1 - 1) \\ sin\delta_2(cos\delta_1 - 1) \\ 0 \end{bmatrix} \quad (2)$$

where $[I, Q, U, V]^T$ is the output Stokes vector, $[I_s, Q_s, U_s, V_s]^T = [1, 1, 0, 0]^T$ is the input Stokes vector of linearly polarized light, and δ_1 and δ_2 are the phase retardations of the LCs. Following Eq. (1) and Eq. (2), the retardance was simulated. Theoretical results confirmed the behavior of the iNC was identical to that of a linear polarizer (Figure S2). To experimentally characterize the polarizer performance, the phase retardations, δ_1 of LC_1 and δ_2 of LC_2 were controlled by applying voltages,

V_{LC1} and V_{LC2}. As the phase retardations were dependent on the applied voltages, we experimentally measured the exact polarization directions at each applied voltage. The dependence of the applied voltages on the transmission polarization axis ϑ showed linearity from 0° to 180° (Figure 2). We then placed the iNC after a linear polarizer (Figure S4). The angle α between the transmission axes of the iNC and the linear polarizer was initially set to be orthogonal. The polarizer mode was achieved by simultaneously tuning both phase retardations δ_1 and δ_2, which depend on the applied voltages, V_{LC1} and V_{LC2}. When we tuned both V_{LC1} (3.05V to 11.9 V) and V_{LC2} (3.58V to 11.6V) of the iNC, the transmission intensity I_{trans} was directly proportional to $cos(2\alpha)$. Matching with Malus's law, experimental results demonstrated the iNC operation was identical to that of a linear polarizer (Figure 2). To experimentally characterize the temporal performance (Figure S5), actuation voltages corresponding to perpendicular (off-state) and parallel (on-state) polarization were applied. The iNC demonstrated a rapid turn-on and-off response time of 25 and 50 ms, respectively (Figure 2), showing potential for rapid imaging. To image plasmonic nano-objects, the iNC was aligned in the detection path. As a representative model of plasmonic nano-objects, we used gold nanorods due to the asymmetric geometry and enhanced scattering as a result of the collective oscillation of electron density of at the metal dielectric interface. For imaging single gold nanorods, the applied voltages V_{LC1} and V_{LC2} were rapidly modulated to switch the transmission polarization from parallel and perpendicular. As a result, the scattering intensity of a gold nanorod was periodically modulated between bright and dark states over time (Figure 2).

Spatially enhanced nanoimaging can be achieved by modulating polarization using the iNC (Figure 3). We imaged single nano-objects (gold nanorods) over a range of polarization ϑ from 0° to 180°. When a mechanically rotated polarizer was used to rotate the polarization from 0° to 180°, the Airy patterns of the imaged nano-objects followed a spiral trace (red curve) exhibiting a $\sin(\vartheta/2)$ behavior due to beam deviations arising from rotating optics. In the magnified images, a red arrow indicates its center at 175°, and a red cross-hair indicates its center at 0°. Each nano-object was

displaced due to beam deviations. In contrast, the iNC corrects for beam deviations. With the iNC, we observed the Airy patterns of the imaged nano-objects followed a straight trace (blue line). For each nano-object, a blue arrow indicates its center at 175°, and a red cross-hair indicates its center at 0°, showing positions of nano-objects remained the same with the iNC. For quantitative characterization, the root-mean-square deviation (RMSD) of each pixel was calculated between the intensity of the pixels at different polarization directions and a fitted sinusoidal function. With a mechanically rotated polarizer, large RMSD was observed due to beam deviations and subsequent loss of spatial information from finite CCD sampling. Conversely, we observed small RMSD with the iNC, indicating successful correction of beam deviations. When spatial errors (1,300 nm) reach the same order of magnitude as the diameter of the Airy patterns (full width half maximum FWHM = 850 nm) as well as the pixel size (170 nm), positional information is substantially obscured and direct visualization of the proximal nano-objects from their far-field Airy patterns becomes infeasible.

Correction of beam deviations by iNC gives rise to accurate and precise spatial information, allowing us to directly observe and distinguish segregated Airy patterns of proximal nano-objects without post image processing (Figure 3). With beam deviations corrected, a single nano-object remained at the same position as the polarization was modulated by the iNC. With beam deviations corrected for proximal nano-objects, positions of Airy patterns corresponding to positions of each nano-object emerged as the polarization was modulated by the iNC. To investigate the precision of iNC, we varied the distance between proximal nano-objects and compared with measurements by scanning electron microscopy. As the distance between proximal nano-objects was varied, we directly observed distances between Airy patterns exactly corresponded to the distances measured by scanning electron microscopy (Figure S6). We also varied the orientation of proximal nano-objects and found that individual Airy patterns can be directly differentiated by their far-field images, enabling positional information to be ascertained in agreement with scanning electron microscopy (Figure S6). We highlight direct observations without post-processing are made possible

by correcting beam deviations below the size of Airy patterns. Such direct observations have the potential to accelerate the acquisition of super-resolution images.

2.2. Spatially enhanced nanomanipulation by iNC

Super-resolution imaging integrated with manipulation of nano-objects should advance dynamical studies. Optical trapping of plasmonic nano-objects has been extensively demonstrated[31–35], however, not in the context of real-time super-resolution. The iNC integrates trapping and manipulation of plasmonic nano-objects using the power modulator mode (Eq. 3 and Eq. 4) and polarization rotator mode (Eq. 5 and Eq. 6), respectively.

iNC power modulator

$$\begin{bmatrix} I \\ Q \\ U \\ V \end{bmatrix} = \frac{1}{2}\begin{bmatrix} 1 & -cos\delta_1 & -sin\delta_1 & 0 \\ 0 & 0 & 0 & 0 \\ -1 & cos\delta_1 & sin\delta_1 & 0 \\ 0 & 0 & 0 & 0 \end{bmatrix}\begin{bmatrix} I_s \\ Q_s \\ U_s \\ V_s \end{bmatrix} \tag{3}$$

$$= \frac{1}{2}\begin{bmatrix} 1 - cos\delta_1 \\ 0 \\ -1 + cos\delta_1 \\ 0 \end{bmatrix} \tag{4}$$

iNC polarization rotator

$$\begin{bmatrix} I \\ Q \\ U \\ V \end{bmatrix} = \frac{1}{2}\begin{bmatrix} 1 & 0 & -1 & 0 \\ -cos\delta_2 & 0 & cos\delta_2 & 0 \\ -sin\delta_2 & 0 & sin\delta_2 & 0 \\ 0 & 0 & 0 & 0 \end{bmatrix}\begin{bmatrix} I_s \\ Q_s \\ U_s \\ V_s \end{bmatrix} \tag{5}$$

$$= \frac{1}{2}\begin{bmatrix} 1 \\ -cos\delta_2 \\ -sin\delta_2 \\ 0 \end{bmatrix} \tag{6}$$

Theoretical results show the power modulation mode can be achieved in a linear regime (Figure S7) while the polarization rotator mode can rotate the the polarization state of light with respect to the retardance (Figure S8). To experimentally demonstrate the iNC in the power modulator mode, we placed the iNC after a fixed linear polarizer and increased V_{LC1} from 3V to 5.5V and fixed V_{LC2} at 3.3V (Figure S9). By tuning V_{LC1}, the transmission power intensity can be adjusted. Figure 4b i shows the transmission power intensity (I) changes by varying V_{LC1} at constant V_{LC2} = 3.3V across a range of wavelengths λ. As I increased with V_{LC1}, a linear response was observed between V_{LC1} = 3.8V and 4.8V. This consistent linear response of I was obtained regardless of the wavelength of incident light from 630 to 690 nm which allows for compatibility of iNC with nano-objects of varying sizes and geometries. To experimentally demonstrate the iNC in the polarization rotator mode, the iNC was then positioned between two fixed linear polarizers (Figure S10). To operate in the polarization rotator mode, V_{LC1} was fixed and V_{LC2} was varied. We constructed a calibration curve of polarization rotation angle ξ as a function of different voltages V_{LC2} from 3.3V to 11.4V. The calibration curve in Figure 4b ii was consistent across wavelength for versatility with various nano-objects.

With the iNC in the power modulation mode, beam deviations can be corrected for spatially enhanced optically trapping. We firstly characterized the real-time performance of the iNC in the power modulator mode. To detect the position in real-time, the iNC was placed after a quadrant position detector (Figure S11) and we measured turn-on and turn-off response times of 25 ms and 50 ms, respectively (Figure 4c). We were able to rapidly adjust the trapping power in 50 ms, allowing for rapid optical trapping manipulation. To optically trap plasmonic nano-objects (gold nanorods), we placed the iNC in the trapping beam path (Figure 4). Tuning V_{LC1} allowed for different trapping powers, resulting in different trapping stiffness. Using the iNC, we modulated the trapping beam power from 30 mW to 90 mW. To achieve highly stabilized particle trapping, the trapping force must

overcome Brownian motion, since Brownian motion is dominant in solution. The position of the nano-object was measured by acquiring a distribution of positional probability using a quadrant position detector. We observed that higher trapping powers (90 mW) resulted in narrower spatial distributions, indicating more stable trapping. With beam deviations corrected, we also directly measured the spatial distribution of position of the nano-object as the trapping beam power was modulated from 30 mW to 90 mW. It can be seen that the distribution of the positions decreased as the power increased (Figure 4c, left inset). Notably, the mean positions remained the same as the trapping beam power was modulated from 30 mW to 90 mW (Figure 4c, right inset), showing there is no deviation of the trapping beam using the iNC. These results support successful correction of beam deviations by iNC for spatially enhanced optical trapping. Rapid rotation of the trapped plasmonic nano-objects (gold nanorods) can be then achieved using the polarization rotator mode of the iNC. In this mode, the iNC showed a turn-on response time of 23 ms and a turn-off response time of 72 ms (Figure 4d). To rotate trapped plasmonic nano-objects, the iNC was in the trapping beam path. As long as the nano-object is resonant with incident light, it will tend to align along the light incident polarization. Thus, the trapped nano-object rotates following the polarization direction. By varying V_{LC2} from 3.3V to 11.4V, the linearly polarized trapping beam changed its polarization direction, causing the trapped nano-object (gold nanorod) to rotate. Using a polarizer/analyzer technique, the intensity of scattered light from a nanorod after a fixed analyzer was recorded with CCD. We observed that the intensity was lowest when the nanocrystal rotated to the position perpendicular to the analyzer and highest when the nanocrystal fully aligned with the analyzer (Figure 4d). Taken together, these results demonstrate precise trapping and rapid rotation of plasmonic nano-objects by the iNC. The iNC could be used in other applications[31–35] where spatially enhanced nano-imaging and nanomanipulation of plasmonic nano-objects may be beneficial.

3. Conclusion

In conclusion, we demonstrated a multimodal iNC for spatially enhanced nanoimaging and nanomanipulation. To operate the iNC in the polarizer mode, both V_{LC1} and V_{LC2} were tuned. To operate in the power modulator mode, V_{LC1} was tuned and V_{LC2} was fixed. To operate in the polarization rotator mode, V_{LC1} was fixed and V_{LC2} was tuned. We demonstrated spatially enhanced nanoimaging by iNC. Using the iNC in the polarizer mode, we showed that correction of beam deviations enabled direct visualization of proximal plasmonic nano-objects below the diffraction limit without post-processing. Such direct observations have the potential to accelerate the acquisition of super-resolution images to allow for integration with optical manipulation. We demonstrated spatially enhanced nanomanipulation by iNC. Using the iNC in the power modulator mode and polarization rotator mode, we showed that correction of beam deviations results in precise trapping and rapid rotation of plasmonic nano-objects. This method can be applied to any nano-object exhibiting polarization anisotropy. In the future, the iNC can be applied to nano-objects of a variety of materials[13,36,37] and geometries[38–40]. This work opens the way for real-time super-resolution imaging integrated with active control.

4. Experimental Section/Methods

Nanoimaging

A darkfield microscope (IX73, Olympus) was configured with a dry condenser (U-DCD, Olympus), a 50x objective (LMPLFLN50XBD, Olympus), a CCD camera (ORCA II,

Hamamatsu) and iNC in the detection path. Both V_{LC1} and V_{LC2} were tuned from 3V to 13.5V and from 3.3V to 11.4V synchronously to modulate the polarization from 0 degree to 175 degree in 5-degree increments. An image was taken at each increment.

For comparison, a linear polarizer (LPVISE200-A, Thorlabs) was placed between the output of the microscope and the camera as a standard, mechanical case. The linear polarizer was manually rotated 180 degrees in 5-degree increments. An image was taken at each increment.

The images were taken at the same transmission polarization angles. In both cases, the CCD camera was placed ~50 mm after the optical elements. The location of the nanorod (center of the Gaussian beam) on the images was determined by Trackmate in ImageJ Fiji[41,42]. The tracking detector was set to be LOG (Laplacian of Gaussian) for Gaussian beam detection.

The iNC was actuated automatically using a function generator (Instek, AFG2225) and DAQ board (NI, PCI6733) with periodically changing voltage levels. Each actuation period consisted of 25 voltage levels (3V to 13.5V and 3.3V to 11.4 V) corresponding to polarization angles from 0 degree to 170 degrees with 7 degree intervals. For a single period, each voltage level lasted 250 ms.

Nanomanipulation

An optical trapping system was configured with a 830 nm cw Ti:Sapphire laser (Spectra Physics 3900s) and a darkfield microscope (Olympus IX73) outfitted with a 60x water immersion objective (Olympus LUCPLFLN60XPH) and iNC in the illumination path. With the iNC in the power modulation mode, the position of optically trapped gold nanorod (100 nm x 30 nm) was measured by placing a QPD (PDQ80A, Thorlabs) at the conjugate back focal plane of the objective. The spatial

position was measured at three different transmission power (30 mW, 60 mW and 90 mW) before the beam entered the objective. The spatial position probability function was calculated by fitting the measured voltages to a probability density function, followed by integration over a finite step size.

With the iNC in the polarization rotator mode, single gold nanorods (100 nm x 30 nm) were suspended in water was trapped using the optical trapping system. By applying V_{LC2} from 3V to 13.5V while V_{LC1} was held constant at 3.3V, the polarization rotation angle was rotated from 0 to 175 degrees repeatedly to rotate the nanorod (two cycles lasting ~72 s). A fixed linear polarizer was placed at the detection port of the microscope to modulate the AuNR intensity to avoid depolarization effects at the sample plane[43,44]. The scattering signal of the nanorod was then captured by a CCD (Thorlabs 1645C). The intensity of the nanorod at different rotational orientations was obtained by averaging the center pixels of the nanorod images with an ROI slightly larger than the FWHM of the gaussian pattern.

Supporting Information

Supporting Information is available from the Wiley Online Library.

Acknowledgements

This work was supported by the National Science Foundation (NSF 1454188), Air Force Office of Scientific Research (AFOSR FA9550-16-1-0272, FA9550-19-1-0186), and academic research fund at the University of Michigan.

Received: ((will be filled in by the editorial staff))
Revised: ((will be filled in by the editorial staff))
Published online: ((will be filled in by the editorial staff))

References

[1] S. Tong, B. Moyo, C. M. Lee, K. Leong, G. Bao, *Nat. Rev. Mater.* **2019**, *4*, 726.

[2] O. M. Maragò, P. H. Jones, P. G. Gucciardi, G. Volpe, A. C. Ferrari, *Nat. Nanotechnol.* **2013**, *8*, 807.

[3] T. A. Klar, S. W. Hell, *Opt. Lett.* **1999**, *24*, 954.

[4] S. W. Hell, M. Kroug, *Appl. Phys. B Lasers Opt.* **1995**, *60*, 495.

[5] M. Hofmann, C. Eggeling, S. Jakobs, S. W. Hell, *Proc. Natl. Acad. Sci. U.S.A.* **2005**, *102*, 17565.

[6] E. Betzig, G. H. Patterson, R. Sougrat, O. W. Lindwasser, S. Olenych, J. S. Bonifacino, M. W. Davidson, J. Lippincott-Schwartz, H. F. Hess, *Science* **2006**, *313*, 1642.

[7] M. J. Rust, M. Bates, X. Zhuang, *Nat. Methods* **2006**, *3*, 793.

[8] T. Dertinger, R. Colyer, G. Iyer, S. Weiss, J. Enderlein, *Proc. Natl. Acad. Sci. U.S.A.* **2009**, *106*, 22287.

[9] C. Sönnichsen, A. P. Alivisatos, *Nano Lett.* **2005**, *5*, 301.

[10] P. Zijlstra, J. W. M. Chon, M. Gu, *Nature* **2009**, *459*, 410.

[11] W. K. Lin, G. Cui, Z. Burns, X. Zhao, Y. Liu, Z. Zhang, Y. Wang, X. Ye, Y. Park, S. E. Lee, *Adv.*

Mater. Interfaces **2021**, *8*, 1.

[12] E. Murphy, Y. Liu, D. Krueger, M. Prasad, S. E. Lee, Y. Park, *Small* **2021**, *2006044*, 1.

[13] M. W. Knight, L. Liu, Y. Wang, L. Brown, S. Mukherjee, N. S. King, H. O. Everitt, P. Nordlander, N. J. Halas, *Nano Lett.* **2012**, *12*, 6000.

[14] J. Perez-Juste, B. Rodriguez-Gonzalez, P. Mulvaney, L. M. Liz-Marzan, *Adv. Funct. Mater.* **2005**, *15*, 1065.

[15] X. Huang, I. H. El-Sayed, W. Qian, M. A. El-Sayed, *Nano Lett.* **2007**, *7*, 1591.

[16] G. Wang, W. Sun, Y. Luo, N. Fang, *J. Am. Chem. Soc.* **2010**, *132*, 16417.

[17] W.-S. Chang, J. W. Ha, L. S. Slaughter, S. Link, *Proc. Natl. Acad. Sci. U. S. A.* **2010**, *107*, 2781.

[18] G. L. Liu, Y. T. Long, Y. Choi, T. Kang, L. P. Lee, *Nat. Methods* **2007**, *4*, 1015.

[19] S. E. Lee, G. L. Liu, F. Kim, L. P. Lee, *Nano Lett.* **2009**, *9*, 562.

[20] S. E. Lee, D. Y. Sasaki, T. D. Perroud, D. Yoo, K. D. Patel, L. P. Lee, **2009**, 14066.

[21] S. E. Lee, D. Y. Sasaki, Y. Park, R. Xu, J. S. Brennan, M. J. Bissell, L. P. Lee, *ACS Nano* **2012**, *6*, 7770.

[22] S. E. Lee, Q. Chen, R. Bhat, S. Petkiewicz, J. M. Smith, V. E. Ferry, A. L. Correia, A. P. Alivisatos, M. J. Bissell, **2015**, DOI 10.1021/acs.nanolett.5b01161.

[23] Y. Liu, Y. Park, S. E. Lee, *Appl. Phys. Lett.* **2016**, *109*, DOI 10.1063/1.4954907.

[24] C. L. Nehl, H. Liao, J. H. Hafner, *Nano Lett.* **2006**, *6*, 683.

[25] O. Schubert, J. Becker, L. Carbone, Y. Khalavka, T. Provalska, I. Zins, C. Sönnichsen, *Nano Lett.* **2008**, *8*, 2345.

[26] A. S. Stender, G. Wang, W. Sun, N. Fang, *ACS Nano* **2010**, *4*, 7667.

[27] Q. Liu, Y. Cui, D. Gardner, X. Li, S. He, I. I. Smalyukh, *Nano Lett.* **2010**, *10*, 1347.

[28] X. Cheng, D. Dai, D. Xu, Y. He, E. S. Yeung, *Anal. Chem.* **2014**, *86*, 2303.

[29] K. H. Møller, I. Trabjerg, *Infrared Phys. Technol.* **2005**, *46*, 351.

[30] D. Clarke, in *Stellar Polarim.*, **2010**, pp. 139–173.

[31] S. E. S. Spesyvtseva, K. Dholakia, *ACS Photonics* **2016**, *3*, 719.

[32] J. Berthelot, S. S. Aćimović, M. L. Juan, M. P. Kreuzer, J. Renger, R. Quidant, *Nat. Nanotechnol.* **2014**, *9*, 295.

[33] L. Shao, Z. J. Yang, D. Andrén, P. Johansson, M. Käll, *ACS Nano* **2015**, *9*, 12542.

[34] K. C. Toussaint, M. Liu, M. Pelton, J. Pesic, M. J. Guffey, P. Guyot-Sionnest, N. F. Scherer, *Opt. Express* **2007**, *15*, 12017.

[35] Y. Y. Tanaka, P. Albella, M. Rahmani, V. Giannini, S. A. Maier, T. Shimura, *Sci. Adv.* **2020**, *6*, 1.

[36] L. Zhang, L. T. Roling, X. Wang, M. Vara, M. Chi, J. Liu, S.-I. Choi, J. Park, J. A. Herron, Z. Xie, M. Mavrikakis, Y. Xia, *Science* **2015**, *62*, 412.

[37] R. Jin, Y. C. Cao, E. Hao, G. S. Metraux, G. C. Schatz, C. A. Mirkin, *Nature* **2003**, *425*, 487.

[38] H.-E. Lee, H.-Y. Ahn, J. Mun, Y. Y. Lee, M. Kim, N. H. Cho, K. Chang, W. S. Kim, J. Rho, K. T. Nam, *Nature* **2018**, *556*, 360.

[39] K. Chandra, K. S. B. Culver, S. E. Werner, R. C. Lee, T. W. Odom, *Chem. Mater.* **2016**, *28*, 6763.

[40] S. E. Lohse, N. D. Burrows, L. Scarabelli, L. M. Liz-Marzán, C. J. Murphy, *Chem. Mater.* **2014**, *26*, 34.

[41] J. Schindelin, C. T. Rueden, M. C. Hiner, K. W. Eliceiri, *Mol. Reprod. Dev.* **2015**, *82*, 518.

[42] J.-Y. Tinevez, N. Perry, J. Schindelin, G. M. Hoopes, G. D. Reynolds, E. Laplantine, S. Y. Bednarek, S. L. Shorte, K. W. Eliceiri, *Methods* **2017**, *115*, 80.

[43] J. B. Lassiter, J. Aizpurua, L. I. Hernandez, D. W. Brandl, I. Romero, S. Lal, J. H. Hafner, P. Nordlander, N. J. Halas, *Nano Lett.* **2008**, *8*, 1212.

[44] M. Atakhorrami, K. M. Addas, C. F. Schmidt, *Rev. Sci. Instrum.* **2008**, *79*, DOI 10.1063/1.2898407.

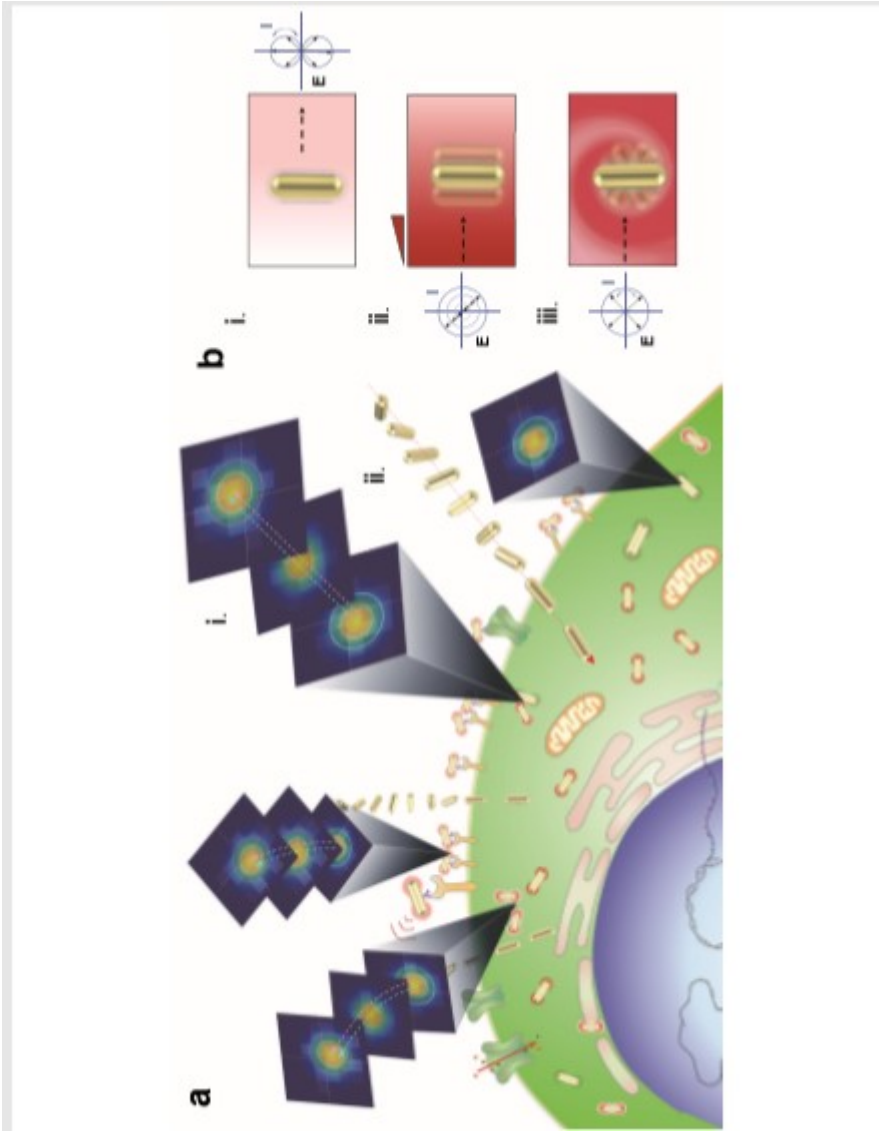

Figure 1. Ultraprecision imaging and manipulation is enabled by integrated nanoscopic correction (iNC). (a) Precise delivery of nano-objects to a desired intracellular location can be enabled by real-time super resolution imaging combined with precise, active control. i. Spatially enhanced nano-imaging without postprocessing by iNC allows for integration with optical manipulation. ii. The iNC enables spatially enhanced nanomanipulation of nano-objects. **(b)** The iNC has multiple modes of operation. i. The iNC in the polarizer mode for spatially enhanced nano-imaging. The iNC in the ii. power modulator mode and iii. polarization rotator mode for spatially enhanced nanomanipulation

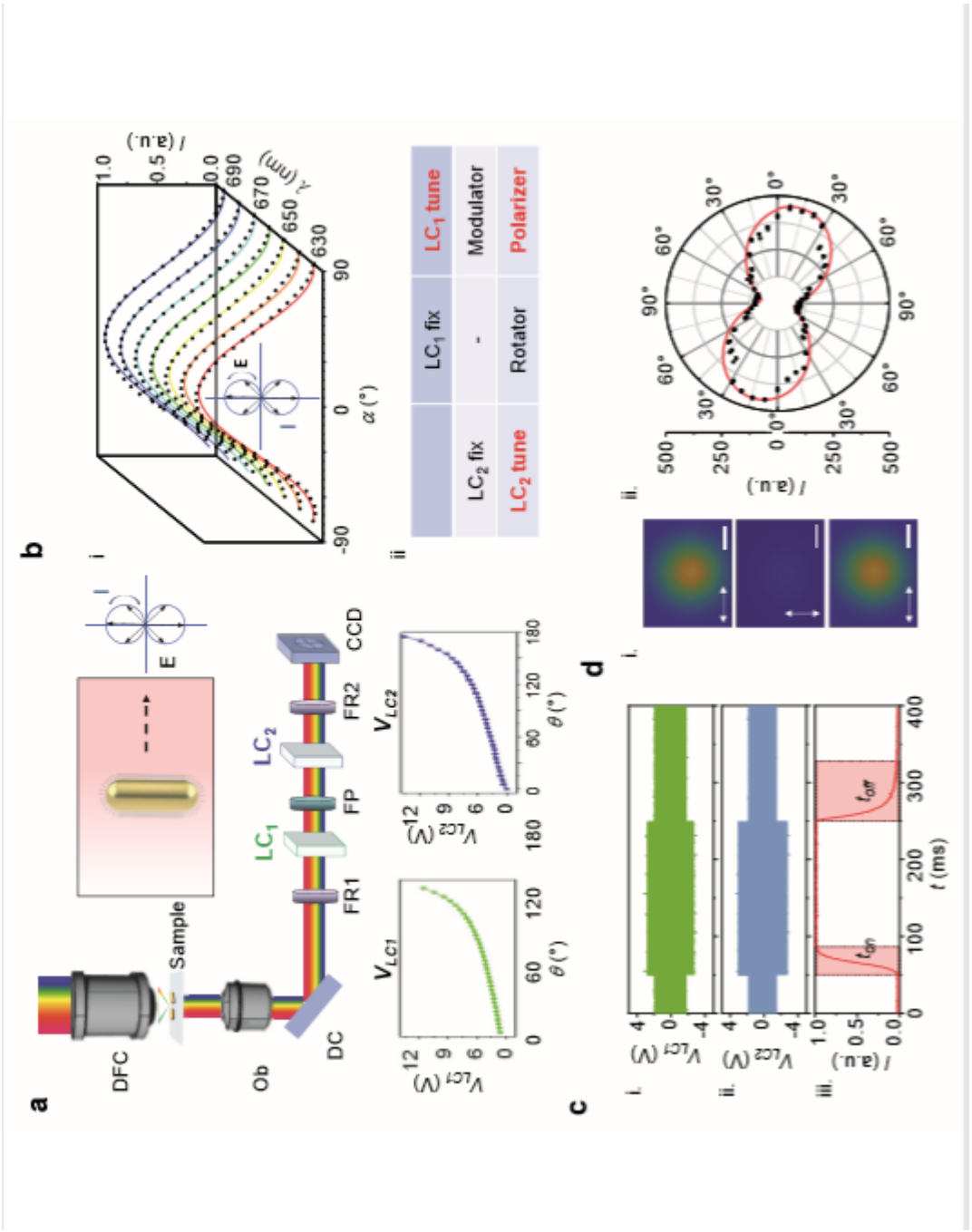

Figure 2. iNC enables spatially enhanced nano-imaging of nano-objects. (a) Conceptual schematic of iNC integrated into a transmission darkfield microscope for nano-imaging (see Supplementary

Information). DFC: darkfield condenser, Ob: objective, DC: dichroic mirror, FR1: fixed retarding layer, LC_1: liquid crystal retarder, FP: fixed polarizing layer, LC_2: liquid crystal retarder, FR2: fixed retarding layer, CCD: charge coupled detector. **(b)** i. The iNC in polarizer mode: Transmission intensity vs. angle α across wavelengths λ following Malus's Law. Angle α is between the transmission axes of the device and a fixed linear polarizer. ii. he iNC operation chart showing iNC in polarizer mode. **(c)** i. Graph of actuation voltage V_{LC1} for LC_1 (green). ii. Graph of actuation voltage V_{LC2} for LC_2 (blue). iii. Graph of response time of iNC in polarizer mode, where t_{on} is the turn-on response time and t_{off} is the turn-off response time. **(d)** i. Images of nanorod at varying transmission polarization using iNC. Scale bar: 470 nm. ii. Polar diagram of scattering intensity as a function of transmission polarization by iNC at peak wavelength 650 nm.

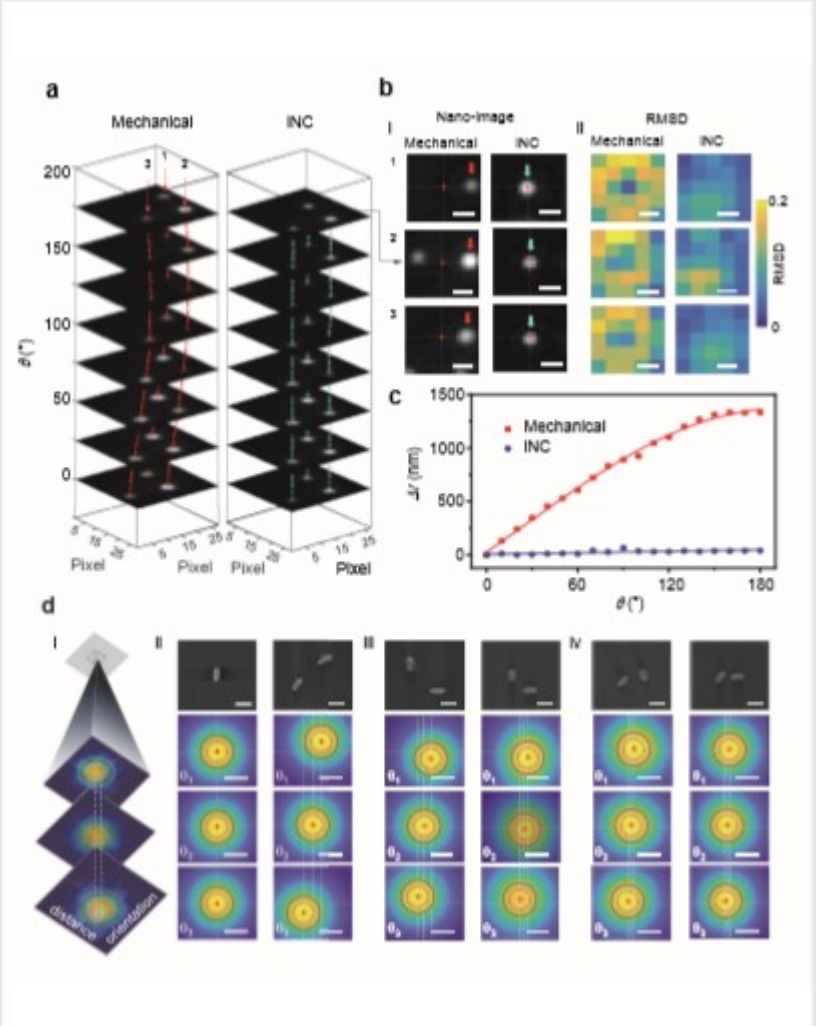

Figure 3. Nanometer spatial stability of iNC facilitates direct observation below diffraction limit. **(a)** Images over transmission polarization using conventional polarizer. ii. Images over transmission polarization using iNC. **(b)** i. Magnified images using conventional polarizer corresponding to part a. Magnified images using iNC corresponding to part a. ii. RMSD using conventional polarizer corresponding to part b, i. RMSD using iNC corresponding to part b, i. Scale bar: 1 µm. **(c)** Graph of spatial deviation $\Delta\ell$ over transmission polarization for conventional polarizer vs. iNC. The maximum spatial error (diameter traced by the nanorod image trajectory) was as large as 1,300 nm. **(d)** i.

Conceptual schematic of direct observation below diffraction limit by spatial stability of iNC. ii. Comparison of single versus multiple nanorods: SEM and corresponding images over transmission polarization. iii. Distance variation: SEM and corresponding images over transmission polarization. iv. Angle variation: SEM and corresponding images over transmission polarization. Scale bar: 500 nm.

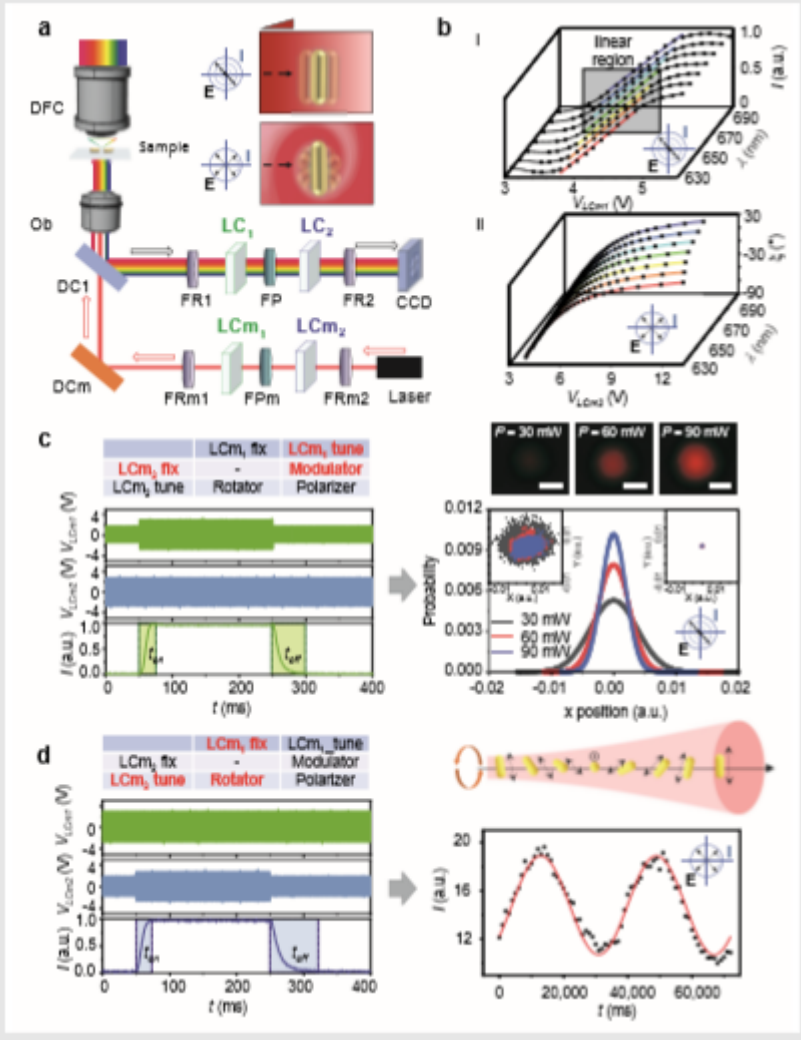

Figure 4. iNC enables spatially enhanced nanomanipulation of nano-objects. (a) Conceptual schematic of iNC integrated into a transmission darkfield microscope for nanomanipulation (see Supplementary Information). DFC: darkfield condenser, Ob: objective, DC: dichroic mirror. (detection path) FR1: fixed retarding layer, LC_1: liquid crystal retarder, FP: fixed polarizing layer, LC_2: liquid crystal retarder, FR2: fixed retarding layer, CCD: charge coupled detector. (trapping beam path) FRm1: fixed retarding layer, LCm_1: liquid crystal retarder, FPm: fixed polarizing layer, LCm_2: liquid crystal retarder, FRm2: fixed retarding layer. **(b)** i. The iNC in power modulation mode: Graph of transmission intensity as a function of actuation voltage V_{LCm1} across wavelengths λ. ii. The iNC in polarization rotator mode: Graph of polarization rotation angle ξ as a function of actuation voltage V_{LCm2} across wavelengths λ. **(c)** (left) The iNC operation chart showing iNC in power modulation mode. Graphs of actuation voltage V_{LCm1} for LCm_1 (green) and actuation voltage V_{LCm2} for LCm_2 (blue). Graph of response time of iNC in power modulator mode, where t_{on} is the turn-on response time and t_{off} is the turn-off response time. (right) Images of trapping beam as power P was

modulated from 30 mW to 90 mW by iNC. Probability of spatial position of a trapped nanorod measured using QPD as power *P* was modulated by iNC. Scale bar: 620 nm. Left inset shows distribution of the positions decreases as power increases. Right inset shows mean positions at each power level overlap. **(d)** (left)) The iNC operation chart showing iNC in polarizaton rotator mode. Graphs of actuation voltage V_{LCm1} for LCm_1 (green) and actuation voltage V_{LCm2} for LCm_2 (blue). Graph of response time of iNC in polarization rotator mode, where t_{on} is the turn-on response time and t_{off} is the turn-off response time. (right) Conceptual schematic showing iNC rotates the polarization direction of the linearly polarized trapping beam, and resulting trapped nanorod rotates following the polarization direction. Graph of scattering intensity of a rotating nanorod over time.

Table of Contents Summary

Optical manipulation and imaging of nano-objects with nanometer precision is highly desirable for nanomaterial and biological studies due to inherent noninvasiveness. However, time constraints and current segregated experimental systems for nanoimaging and nanomanipulation limits real-time super-resolution imaging with spatially enhanced manipulation. Here, we report an integrated nanoscopic correction (iNC) method to enable multimodal nanomanipulation-nanoimaging.

Yunbo Liu, Zhijia Zhang, Younggeun Park, Somin Eunice Lee

Ultraprecision imaging and manipulation of plasmonic nanostructures by integrated nanoscopic correction (iNC)